Nonlinear Dyn (2023) 111:3099–3112
https://doi.org/10.1007/s11071-022-07997-0

ORIGINAL PAPER

Exploiting surface textures dynamics for dry friction control

N. Menga · **F. Bottiglione** · **G. Carbone**

Received: 11 May 2022 / Accepted: 9 October 2022 / Published online: 20 October 2022

Abstract We study the dynamic behavior of a lattice of bristle-like elastic elements disposed at the interface between a rigid still substrate and a rigid sliding slab, in steady conditions. Due to normal and frictional interactions with the moving slab, complex bristles dynamics occur, which may eventually alter the overall frictional response of the structured interface. Indeed, up to three main mechanisms of friction control can be identified, depending on the specific bristles dynamics: the relative velocity-dependent modulation of local friction force; the misalignment between the local relative velocity and the slab velocity, due to the emergence of transverse vibration; the local friction coefficient variation due to the normal load acting on the bristle. Results show that, depending on the interface dynamic properties (i.e., bristles stiffness, normal load, slab velocity, etc.), a significant reduction of the friction force opposing the slab motion can be achieved, also involving self-excited bristle vibration. Since the present formulation is scale independent, this result may suggest possible mechanisms of friction control in different practical application fields, ranging from bio-inspired micro-structured interfaces to macro-scale features, such as brush seals in electric motors.

Keywords Nonlinear dynamics · Sliding friction · Surface texture · Vibrations · Interface

N. Menga · F. Bottiglione · G. Carbone
Department of Mechanics, Mathematics and Management, Politecnico of Bari, V.le Japigia 182, 70126 Bari, Italy

N. Menga (✉) · G. Carbone
Department of Mechanical Engineering, Imperial College London, Exhibition Road, London SW7 2AZ, UK
e-mail: nicola.menga@poliba.it

G. Carbone
Physics Department "M. Merlin", CNR - Institute for Photonics and Nanotechnologies U.O.S. Bari, via Amendola 173, 70126 Bari, Italy

1 Introduction

The study of the interactions between bodies is one of the most crucial topic in modern applied science. The field of possible interfacial interactions is very broad involving, for instance, interatomic/intermolecular adhesion, chemical links, electrostatic and electromagnetic potentials. Among them, frictional interactions are of primary importance in modern engineering, as these interactions are basically related to energy dissipation. Therefore, controlling the frictional interaction between bodies has always been of great interest, for both micro-, meso-, and macro-scale applications.

Several studies have focused on the frictional response of deformable rough interfaces in relative sliding. Interestingly, most of these studies investigate quasi-static interfacial conditions, where dynamic effect are neglected and gross slip conditions are fully developed. Investigations are performed by exploiting both Boundary Element Methods (BEM) and Finite Element Method (FEM) techniques [1–3], also focusing on hysteretic friction arising due to cyclic defor-

mation in viscoelastic materials during sliding [4–6], and on viscoelastic damping in dynamic systems [7,8]. Moreover, the effect of the tangential deformations of asperities have been recently taken into account [9,10], showing that an additional friction term may arise due to this peculiar feature in thin interfacial coatings.

Furthermore, interfacial sliding friction between rough surfaces may also be affected by the superimposition of *in-plane* microscopic transverse vibrations. The first studies on this topic were focusing on rigid rough interfaces [11,12]. In this case, a friction reduction is predicted, which is mainly ascribed to the vibration-induced misalignment between the interfacial relative velocity and the macroscopic sliding. Since the interface is assumed as rigid, the transverse vibration cannot emerge spontaneously, therefore it has to be forced by an external source of energy. Moreover, a recent experimental investigation on stiff materials (so that surface asperities can be assumed as rigid) has shown that, in order to appreciate a considerable reduction of friction, high-frequency transverse vibrations are required, thus involving a likely huge impact on the overall energy efficiency of the system [13]. On the contrary, deformable rough interfaces offer an additional mechanism of friction reduction, i.e., the dynamic interplay between the static/kinetic friction transition and the asperity shear deformation. Indeed, while in gross sliding the kinetic friction force is strictly prescribed by the specific friction model (e.g., the *Amontons/Coulomb* model), under static friction conditions the actual friction force depends on the overall momentum balance and on the asperity dynamics. In this case, instantaneous very low "static-like" friction may occur. Indeed, due to the non-uniform distribution of gap and normal pressure, rough interfaces may experience a sequences of local stick–slip transitions in the contact domain. Since the contact of rough interfaces can be summarized as the interactions between incommensurate lattices [14,15], where the stick–slip transitions are non-synchronized and non-uniformly distributed, the overall friction at the interface may be lower than the kinetic friction value related to the ideally rigid case. Usually, this phenomenon is modeled by means of dynamic friction models, which are specifically designed in order to take into account for the reaction force caused by the asperity deformation. It is the case of the Dahl friction model [16], which relies on a purely elastic description of the asperity deformation by introducing an equivalent stiffness, and the LeGru friction model, which also encompass an equivalent dashpot to describe the material damping associated with the asperity deformation (see [17] and references therein). A few recent studies have investigated the frictional behavior of sliding rough interfaces in the presence of transverse vibration, estimating the effect of interfacial deformations by means of the aforementioned dynamic friction models [18–20]. It has been shown that a large friction reduction is expected. However, a more accurate description of the dynamic frictional behavior may offer the chance to further extend these investigations. This is the case, for instance, of Refs. [21,22], where the macroscopic frictional response of the interface is calculated averaging the local results over a large population of asperities with different dynamic properties.

Although more accurate than those considering rigid interfaces, these studies still investigate a mechanisms of friction control relying on externally forced transverse vibrations. On the other hand, the development of *in-plane* spring-block models has allowed to simulate the propagation of attachment (and detachment) fronts through the interface. Of course, a lumped (i.e., cantilever) description of the asperity dynamics is required in this case. It is the case, for instance, of Refs. [23,24] where the contact interface is modeled as a regular lattice of Burridge–Knopoff spring-block elements. Results show that, depending on the bulk elasticity of the lattice, the macroscopic friction coefficient may result as low as half of the local one, as the directions of distributed contact ruptures compared to the sliding direction play a key role. Reference [25] extends the previous studies to the case of anisotropic distribution of spring-block elements, showing similar results. Also, in Ref. [26] the *in-plane* dynamics of bristle-like elastic elements has been investigated, assuming a regular lattice in macroscopic sliding conditions against a rigid flat surface. Differently from Burridge–Knopoff spring-block models, bristle-like interfacial features are described as non-interacting spring-mass elements, with both axial and bending deformability, so that self-excited *in-plane* transverse vibration may spontaneously emerge. In addition to the dynamics of contact rupture fronts, this offers a further mechanism of macroscopic friction reduction.

In the present study, we focus on the frictional behavior of 3D bristle-like interfacial features, arranged in a regular lattice. Bristle-like interfacial features are modeled as beam elements, whose dynamic behavior

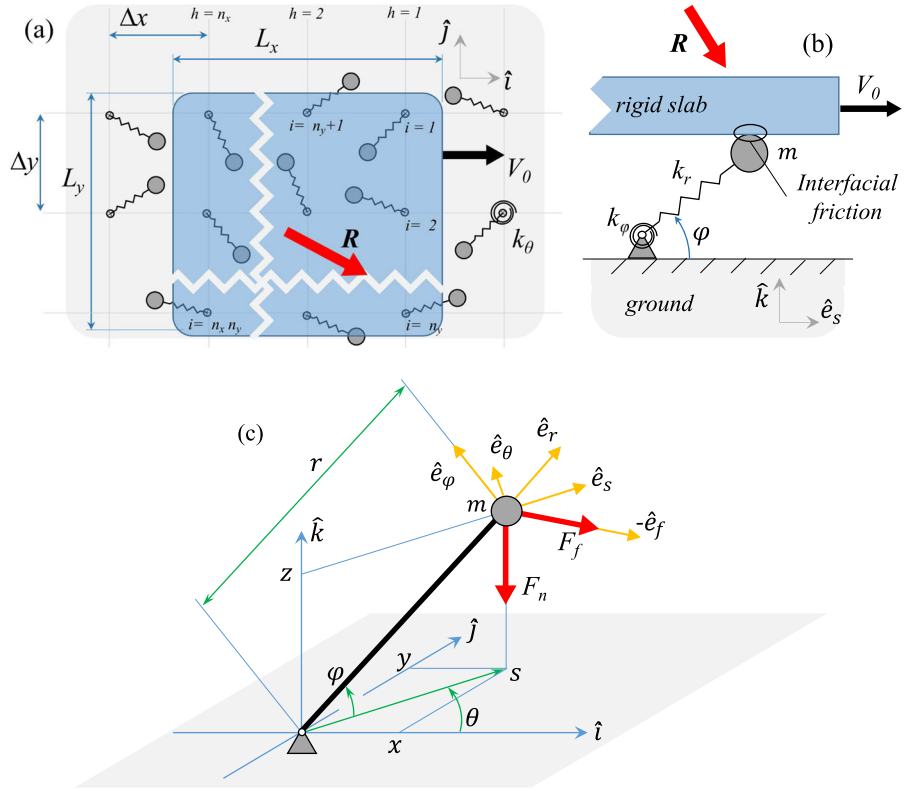

Fig. 1 The schematic of the system at hand: a rigid slab in sliding contact with a lattice of bristle-like elastic elements. A top view (**a**) of the system, showing the azimuthal stiffness k_θ; a side view (**b**) of a generic bristle-like elastic element of mass m, showing the radial and polar stiffnesses k_r and k_φ. A 3D representation (**c**) of the bristle-like element, allowing to appreciate the geometric quantities in the bristle reference frame. Notably, z_0 is the normal gap between the slab and the ground

is modeled as mass-spring-damper systems with axial elongation, and polar and azimuthal bending degrees of freedom. This formulation allows to directly investigate the effect of the features 3D dynamics on the interfacial frictional behavior, also considering the effect of the local distribution of normal load on each bristle and the emergence of *in-plane* and *out-of-plane* self-excited vibration. Possible applications of the results here presented may range from friction reduction in mechanical systems at the macro-scale (e.g., brush seals [27,28]) to bio-inspired functional interface development in micro-/meso-scale systems [29,30].

2 Formulation

As shown in Fig. 1a, in this study we consider the case of a rigid slab sliding at constant velocity V_0, under the action of a force $\mathbf{R}$, over a lattice of elastic bristles (with $\Delta x = \Delta y = \Delta$). Each bristle is modeled as a 3D lumped element. The mass m is localized at the bristle tip, whereas, with reference to Fig. 1c, we define k_r, k_θ, and k_φ as the elastic stiffness of the bristle in the radial, azimuthal, and polar coordinates, respectively. The undeformed length of each element is r_0, whereas the undeformed azimuthal and polar angles are indicated as θ_0 and φ_0, respectively. The bristle damping arising from the bulk polymeric material is modeled by means of lumped dampers, with damping coefficients c_θ and c_φ, acting on the azimuthal and polar components of the bristle angular velocity, respectively.

Moreover, we neglect any interaction between bristles, and between bristles and ground; therefore, each bristle tip is only subjected to normal and *in-plane* frictional forces arising at the contact interface with the rigid moving slab (see Fig. 1c). More in details, we observe that calculations are performed assuming a given normal gap $z_0 < r_0$ between the rigid slab and the ground, so that the equilibrium normal force $R_n = \mathbf{R} \cdot \hat{\mathbf{k}}$ occurring on the moving slab results as the sum of the bristles normal contact forces. However, in the limit of a sufficiently large number N_c of contacting bristles, we expect $R_n(t) = R_n$ in steady sliding conditions, given the value of z_0. Notably, due to bristles deformation, we may have $N_c > N_0 = L_x L_y / \Delta^2$.

According to Fig. 1c, the equation of motion of the bristle can be written as

$$m\ddot{\mathbf{r}} = -k_r(r-r_0)\hat{\mathbf{e}}_r - \frac{1}{s}\left[k_\theta(\theta-\theta_0)+c_\theta\dot{\theta}\right]\hat{\mathbf{e}}_\theta - \frac{1}{r}\left[k_\varphi(\varphi-\varphi_0)+c_\varphi\dot{\varphi}\right]\hat{\mathbf{e}}_\varphi + \mathbf{F}_f + \phi(r)\,\hat{\mathbf{e}}_l + \mathbf{F}_n, \tag{1}$$

where $\mathbf{r} = x\hat{\mathbf{i}} + y\hat{\mathbf{j}} + z\hat{\mathbf{k}} = r\hat{\mathbf{e}}_r$ is the radius vector with $r = \sqrt{x^2+y^2+z^2}$, and $\mathbf{s} = x\hat{\mathbf{i}} + y\hat{\mathbf{j}} = s\hat{\mathbf{e}}_s$ is the in-plane projection of $\mathbf{r}$, with $s = \sqrt{x^2+y^2}$. Moreover,

$$\begin{aligned}
\hat{\mathbf{e}}_r &= \frac{1}{r}(x, y, z),\\
\hat{\mathbf{e}}_\theta &= \frac{1}{s}(-y, x, 0),\\
\hat{\mathbf{e}}_\varphi &= \frac{1}{rs}\left(-xz, -yz, x^2+y^2\right),\\
\hat{\mathbf{e}}_s &= \frac{1}{s}(x, y, 0).
\end{aligned} \tag{2}$$

In order to model the contact interaction between the bristle tip and the rigid slab, in Eq. (1) we adopt a short-range (i.e., hard-wall) repulsive interaction, so that $\mathbf{F}_n = -F_n(z)\,\hat{\mathbf{k}}$ where

$$F_n(z) = \frac{\beta m V_0^2}{2\lambda_z} e^{-(z_0-z)/\lambda_z} \tag{3}$$

with β being a constant of order unity, and $\lambda_z \ll 1$ being a range parameter.

Similarly, the term

$$\phi(r) = \frac{\alpha m V_0^2}{2\lambda} e^{-s/\lambda} \tag{4}$$

in Eq. (1) represents an additional short-range repulsive force necessary to avoid the singular behavior of Eq. (1) in $\mathbf{r} = (0, 0, z)$. Specifically, we assume $\alpha = \beta = 1$ and $\lambda = \lambda_z = 0.001 r_0$.

The term $\mathbf{F}_f$ in Eq. (1) represents the *in-plane* friction interaction occurring between the rigid slab and the bristle head. Specifically,

$$\mathbf{F}_f = -F_f\hat{\mathbf{e}}_f \tag{5}$$

where

$$\hat{\mathbf{e}}_f = \frac{\mathbf{V}_R}{|\mathbf{V}_R|} \tag{6}$$

with $\mathbf{V}_R = (\dot{x} - V_0)\,\hat{\mathbf{i}} + \dot{y}\hat{\mathbf{j}}$ being the *in-plane* relative velocity between the bristle and the rigid slab (notably, $V_R = |\mathbf{V}_R|$). Since the bristle is modeled as an elastic body, the dependence of the friction force on the bristle deformation is intrinsically provided by Eq. (1). In rigid body simulations, this task is accomplished by dynamic friction models, such as the Dahl model [16]. On the contrary, for a proper description of the bristle dynamics, a key feature is the transition from static ($V_R = 0$) to kinetic friction occurring as $V_R > 0$. In the original Coulomb model, this is nominally associated with a friction force discontinuity. However, in real applications, such a discontinuity is actually smoothened due to several speed-dependent phenomena occurring at the interface (e.g., material elastic/viscoelastic deformability, intermolecular bonding/debonding process, etc.) [14,31,32], therefore a "regularized," or "continuous," speed-dependent non-monotonic friction model is commonly assumed [17,33,34]. Specifically, in agreement with Refs. [35–37], we define a speed-dependent characteristic function in the form

$$\chi(V_R) = A\sin\left(B\tan^{-1}\left\{V_R/V_s - C\left[V_R/V_s - \tan^{-1}(V_R/V_s)\right]\right\}\right), \tag{7}$$

where A and C are empirical coefficients, and $B = 2\left[1 - \sin^{-1}(1/A)/\pi\right]$. Notably, V_s is the so-called threshold speed between static and kinetic friction. We observe that Eq. (7) prescribes vanishing friction for $V_R \to 0$, whereas for $V_R \gg V_s$ the kinetic friction plateau is achieved (see Ref. [26]).

In terms of specific friction models, we compare two different cases. The first one is the well-known *Amontons-Coulomb* model, with

$$F_f = \chi(V_R)\,\mu_c F_n \tag{8}$$

where μ_c is the kinetic friction coefficient.

The second case, also referred to as *Nominal Shear Stress* (NSS) model [30,38,39], mostly applies to relatively soft polymers where the frictional shear stress τ_f can be assumed uniform on the contact area A_c and independent of the applied normal load, so that

$$F_f = \chi(V_R)\,\tau_f A_c \tag{9}$$

In this case, since the bristle tips are spherical cups of radius R_c, Hertzian contact mechanics can be employed to calculate the effective contact area A_c between the tips and the rigid slab. Indeed,

$$A_c = \pi\left(\frac{3R_c F_n}{4E^*}\right)^{2/3} \tag{10}$$

where $E^* = E/\left(1-\nu^2\right)$, with E and ν being the Young modulus and Poisson's ratio of the bristles material, respectively.

Finally, in Eq. (1), the damping coefficients take the form

$$c_\theta = \zeta_\theta c_{\theta,cr}$$
$$c_\varphi = \zeta_\varphi c_{\varphi,cr} \tag{11}$$

where ζ_θ and ζ_φ are the damping ratios, and

$$c_{\theta,cr} = 2\sqrt{k_\theta m \left(r_0 \cos\varphi_0\right)^2}$$
$$c_{\varphi,cr} = 2\sqrt{k_\varphi m r_0^2} \tag{12}$$

are the linearized critical damping coefficients for the azimuthal and polar degrees of freedom. Notably, we neglect any other source of damping, such as that arising from bristles collision and rebound. Indeed, we assume the contact size between the bristle heads and the moving slab to be sufficiently small to neglect any viscoelastic damping associated with the impact dynamics.

2.1 Dimensionless quantities and closing equations

Equation (1) can be made non-dimensional by adopting the following dimensionless parameters: $\tilde{k}_r = r_0^2 k_r / \left(m V_0^2\right)$, $\tilde{k}_\theta = k_\theta / \left(m V_0^2\right)$, $\tilde{k}_\varphi = k_\varphi / \left(m V_0^2\right)$, $\tilde{c}_\varphi = c_\varphi / \left(m V_0 r_0\right)$, $\tilde{c}_\theta = c_\theta / \left(m V_0 r_0\right)$, $\tilde{\tau}_f = \tau_f r_0^3 / \left(m V_0^2\right)$. Moreover, the forces are made non-dimensional by the factor $r_0 / \left(m V_0^2\right)$, the lengths by the factor $1/r_0$, and the dimensionless time is $\tilde{t} = t V_0 / r_0$. Therefore, we have that $\tilde{\mathbf{a}} = \ddot{\mathbf{r}} r_0 / V_0^2$ is the dimensionless acceleration, and $\theta' = d\theta/d\tilde{t} = \dot{\theta} r_0 / V_0$ and $\varphi' = d\varphi/d\tilde{t} = \dot{\varphi} r_0 / V_0$ are the dimensionless components of the bristle angular velocity.

After some algebra, Eq. (1) takes the form

$$\tilde{\mathbf{a}} = -\tilde{k}_r(\tilde{r} - 1)\hat{\mathbf{e}}_r - \frac{1}{\tilde{s}}\left[\tilde{k}_\theta(\theta - \theta_0) + \tilde{c}_\theta \theta'\right]\hat{\mathbf{e}}_\theta - \frac{1}{\tilde{r}}\left[\tilde{k}_\varphi(\varphi - \varphi_0) + \tilde{c}_\varphi \varphi'\right]\hat{\mathbf{e}}_\varphi + \tilde{\mathbf{F}}_f + \tilde{\phi}(r)\,\hat{\mathbf{e}}_l + \tilde{\mathbf{F}}_n \tag{13}$$

Notably, in the case of *Coulomb* friction, we have that

$$\tilde{F}_f = \chi(V_R)\,\mu_c \tilde{F}_n, \tag{14}$$

whereas for NSS friction we have

$$\tilde{F}_f = \chi(V_R)\,\tilde{\tau}_f \tilde{A}_c, \tag{15}$$

with

$$\tilde{A}_c = \frac{A}{r_0^2} = \pi\left(\frac{3\tilde{R}_c \tilde{F}_n}{4\tilde{E}^*}\right)^{2/3} \tag{16}$$

where $\tilde{R}_c = R_c / r_0$ and $\tilde{E}^* = E^* r_0^3 / \left(m V_0^2\right)$.

In order to solve Eq. (13), two additional closing equations are required to enforce the congruence between $\mathbf{r}(t)$ and the angles $\theta(t)$ and $\varphi(t)$. These can be easily derived as first-order ODE, thus

$$\theta' = \frac{\tilde{x}\tilde{v}_y - \tilde{y}\tilde{v}_x}{\tilde{r}^2} \tag{17}$$

$$\varphi' = \frac{1}{\sqrt{\tilde{x}^2 + \tilde{y}^2}}\left(\tilde{v}_z - \tilde{z}\frac{\tilde{x}\tilde{v}_x + \tilde{y}\tilde{v}_y + \tilde{z}\tilde{v}_z}{\tilde{x}^2 + \tilde{y}^2 + \tilde{z}^2}\right) \tag{18}$$

with $\tilde{v}_x = \dot{x}/V_0$, $\tilde{v}_y = \dot{y}/V_0$, and $\tilde{v}_z = \dot{z}/V_0$.

2.2 Forces acting on the slab

While sliding over the bristles lattice, the rigid slab is in contact with a certain number N_c of bristle tips. By integrating the equations of motion (13) and the closing equations (17, 18) derived in the previous sections, the dynamics of each bristle can be calculated, so that the time-history of the normal F_n and friction force $\mathbf{F}_f$ occurring at the interface between the bristle and the sliding slab are known. The detailed procedure to derive the steady equilibrium force $\bar{\mathbf{R}}$ acting on the rigid slab in steady sliding conditions is given in "Appendix A."

Notably,

$$R_x = \bar{\mathbf{R}} \cdot \hat{\mathbf{i}}$$
$$R_y = \bar{\mathbf{R}} \cdot \hat{\mathbf{j}}$$
$$R_n = -\bar{\mathbf{R}} \cdot \hat{\mathbf{k}} \tag{19}$$

and, since we are interested in highlighting the effect of the bristles deformability and dynamics on the possible reduction of the global friction force opposing the slab motion, we define the normalized friction force components as

$$\check{R}_x = \frac{R_x}{R_{\text{rigid}}} \tag{20}$$

$$\check{R}_y = \frac{R_y}{R_{\text{rigid}}} \tag{21}$$

where R_{rigid} is the overall friction force corresponding to the limiting case of rigid bristles at the interface. Notably, R_{rigid} depends on the specific friction model postulated at the interface. Indeed, for the *NSS* friction model, using Eqs. (9, 10) we have

$$R_{\text{rigid}}^{\text{NSS}} = N_{c,0}\tau_f \pi \left(\frac{3R_c}{4E^*}\frac{R_n}{N_{c,0}}\right)^{2/3}; \tag{22}$$

whereas, for the *Amontons-Coulomb* friction model, using Eq. (8) we have

$$R_{\text{rigid}}^{C} = \mu_c R_n \tag{23}$$

3 Results

As shown in the previous section, the bristles dynamics is governed by nonlinear equations of motion, therefore we expect the dimensionless elastic parameters and the local frictional behavior to play a key role . The range of possible values of such parameters span over orders of magnitude, depending on the actual bristles geometry and material; however, since this study aims at qualitatively highlighting the possible mechanisms of friction reduction in real-life applications, we explore a parameters range close to the values related to existing bristle-like interfaces, such as those of low-friction artificial ski slopes [40]. Specifically, without any loss of generality of the presented dynamic model, we assume $r_0 = 17$ mm, $R_c = 1$ mm. Moreover, in the framework of linear beam elasticity, due to the bristle bending, one can estimate $k_\varphi \approx k_\theta \approx 3\pi E R^4/4r_0$ and $k_r \approx 10k_\varphi$. Assuming polymeric bristles (e.g., $E \approx 10^2$ MPa and $\nu \approx 0.4$) with $m \approx 10^{-4}$ kg, and slab sliding velocity $V_0 = 10$ m/s, we have $\tilde{k}_\varphi \approx \tilde{k}_\theta \approx 1$, $\tilde{k}_r \approx 10$. We also assume $\zeta_\theta = \zeta_\varphi = 0.1$, $\Delta = 0.2r_0$, and $L_x = L_y = 5r_0$.

Furthermore, since the initial orientation θ_0 of each bristle may depend on many factors (e.g., fabrication techniques, bristle buckling under normal load, etc.), we assume the values of θ_0 to be randomly distributed in the interfacial lattice. As already shown in Ref. [26], for a sufficiently large value of N_c, this leads to *in-plane* isotropic lattice response and to $R_y = 0$. In the same study, quantitative insights have been provided about the effect of non-uniform distributions of θ_0 among the bristle lattice.

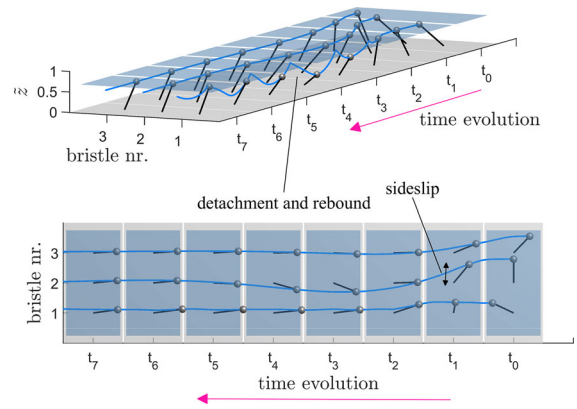

Fig. 2 A qualitative representation of the time-history of three bristles with different initial orientation θ_0. Notably, at time t_0, t_1, and t_2, low relative velocity occurs at the bristle–slab interface

3.1 NSS model

In this section, we present the bristles dynamics and the frictional response of the structured interface assuming *NSS* local friction model. In agreement with Ref. [38], we estimate $\tilde{\tau}_f = 3 \times 10^4$.

In this case, we identify three different mechanisms able to alter the instantaneous friction regime at the bristle tip-sliding slab interface. Consequently, we define three dimensionless integral parameters calculated from the time-history of the i-th bristle and, then, averaged among the whole set of bristles in contact. Therefore, we have

$$\tilde{\gamma}_1 = \left\langle \frac{\int_0^{\Delta\xi_i} d\xi\, F_n(\xi)\, \chi\left(V_R(\xi)\right)}{\int_0^{\Delta\xi_i} d\xi\, F_n(\xi)} \right\rangle_i \tag{24}$$

to take into account the effect of the modulation of the friction force, according to Eq. (7), depending on the modulus of the relative velocity V_R between the i-th bristle tip and the slab;

$$\tilde{\gamma}_2 = \left\langle -\frac{\int_0^{\Delta\xi_i} d\xi\, F_n(\xi)\left(\hat{\mathbf{e}}_f(\xi)\cdot\hat{\imath}\right)}{\int_0^{\Delta\xi_i} d\xi\, F_n(\xi)} \right\rangle_i \tag{25}$$

to quantify the effect of transverse vibration (i.e., sideslip in Fig. 2) with respect to the direction of the slab motion (i.e., $\hat{\imath}$);

$$\tilde{\gamma}_3 = \left\langle \frac{\frac{1}{\Delta\xi_i}\int_0^{\Delta\xi_i} d\xi\, F_n(\xi)^{2/3}}{\left[\frac{1}{\Delta\xi_i}\int_0^{\Delta\xi_i} d\xi\, F_n(\xi)\right]^{2/3}} \right\rangle_i \tag{26}$$

to capture the effect of the instantaneous contact area size at the bristle tip-rigid slab interface as a function

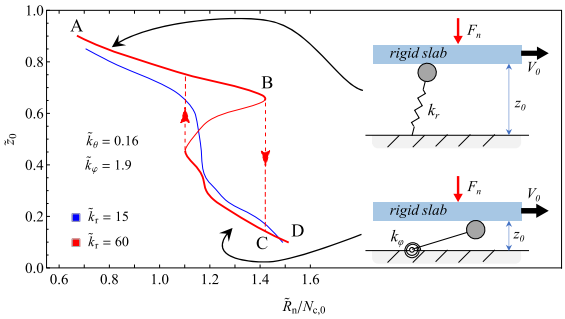

Fig. 3 The normalized dimensionless slab sliding height $\tilde{z}_0$ as a function of the dimensionless normal force $\tilde{R}_n/N_{c,0}$ acting on the sliding slab. Dashed lines represent the hysteretic limiting circle associated with blisters nonlinear bending behavior. The thick line represents the stable conditions. Schematics on the right represent qualitative blisters deformation mechanisms associated with different $\tilde{z}_0$ values (i.e., compression for $\tilde{z}_0 \to 1$, and bending for $\tilde{z}_0 \to 0$). Notably, $\tilde{R}_n = R_n r_0/\left(mV_0^2\right)$

of the normal force $F_n\,(t)$ acting on the i-th bristle (see Eq. (10)). Notably, in Eqs. (24–26), $\Delta\xi_i$ represents the total contacting time of the i-th bristle against the rigid moving slab (see "Appendix A"), whereas, the symbol $\langle\rangle_i$ indicates the ensemble average over the whole set of bristles in contact.

Figure 3 shows the normalized dimensionless normal force $\tilde{R}_n/N_{c,0}$ acting on the slab as a function of the dimensionless gap $\tilde{z}_0$, for different values of the bristle dimensionless radial stiffness $\tilde{k}_r$. Interestingly, regardless of the specific value of $\tilde{k}_r$, three different regimes can be defined. At both very large and very low values of $\tilde{R}_n/N_{c,0}$, linear trends are reported between the normal force and the slab sliding height, with different slopes. Indeed, for $\tilde{z}_0 \to 1$, the main deformation mechanism of the bristle is the axial compression (mainly governed by $\tilde{k}_r$), and the normal behavior turns out very stiff. On the other hand, for $\tilde{z}_0 \to 0$, bristle bending occurs in the polar plane, so that $\tilde{R}_n/N_{c,0}$ is proportional to $\tilde{k}_\varphi$. At intermediate values of the dimensionless normal force $\tilde{R}_n/N_{c,0}$, a nonlinear trend of $\tilde{z}_0$ is reported. In this regime, depending on the specific value of the elastic parameters (i.e., $\tilde{k}_r$, $\tilde{k}_\theta$, and $\tilde{k}_\varphi$), unstable branches can be identified in the $\tilde{R}_n/N_{c,0}$ vs $\tilde{z}_0$ equilibrium curve which, in case of oscillations of the normal force $\tilde{R}_n$ acting on the slab, may lead to hysteretic cycles (see the dashed lines in Fig. 3). In this reference, for each set of elastic parameters, we consider a monotonically increasing loading transient phase until the target normal load is reached; therefore, in case of non-monotonic $\tilde{R}_n/N_{c,0}$ vs $\tilde{z}_0$ trends (i.e., red curve in Fig. 3), the stable equilibrium branch corresponds to the A-B-C-D path shown in Fig. 3. Notably, we observe that, depending on the specific value of $\tilde{R}_n/N_{c,0}$, the effect of $\tilde{k}_r$ on the value of $\tilde{z}_0$ at equilibrium may significantly change as, at low values of $\tilde{R}_n/N_{c,0}$ the larger the value of $\tilde{k}_r$, the larger the value of $\tilde{z}_0$ at equilibrium, whereas at low values of $\tilde{R}_n/N_{c,0}$ the scenario is reversed.

The main results, in terms of frictional behavior of the blisters array, are shown in Fig. 4. Specifically, Fig. 4a shows the normalized friction force component $\check{R}_x^{\mathrm{NSS}}$ opposing the slab motion as a function of both the dimensionless radial and azimuthal stiffness $\tilde{k}_r$ and $\tilde{k}_\theta$. Similarly, Fig. 4b–d reports, respectively, the $\tilde{\gamma}_1$, $\tilde{\gamma}_2$, $\tilde{\gamma}_3$ dimensionless parameters as functions of $\tilde{k}_r$ and $\tilde{k}_\theta$. We observe that increasing the value of $\tilde{k}_r$ leads to lower normalized friction force $\check{R}_x^{\mathrm{NSS}}$ opposing the slab motion, mostly due to the reduction of the effective contact area between the bristles tips and the sliding slab, as suggested by the sharp reduction of the dimensionless parameter $\tilde{\gamma}_3$. Such a result can be qualitatively explained by observing that, according to Fig. 3, increasing $\tilde{k}_r$ may lead to an increase of $\tilde{z}_0$ which roughly represents the lever arm of the friction force F_f acting on each bristle in the l,z plane (see Fig. 1c). In dynamic conditions, this may lead to enhanced bristle oscillations in the l,z plane (see bristle rebound in Fig. 2) and to wider fluctuations in the time-history of the bristle normal force F_n. Since, according to *NSS* friction model [see Eqs. (9, 10)], we have that $F_f\,(t) \propto [F_n\,(t)]^{2/3}$, this leads to a lower normalized friction force component $\check{R}_x^{\mathrm{NSS}}$. Furthermore, increasing $\tilde{k}_r$ also leads to smaller bristles elongation and to a lower number of bristles N_c in contact with the slab at the same time (as shown in Fig. 5a). Since from Eqs. (9, 10), given the normal force R_n acting on the slab, we can estimate $\check{R}_x^{\mathrm{NSS}} \propto \left(N_c/N_{c,0}\right)^{1/3}$, a reduction of N_c also entails lower friction opposing the slab motion. Interestingly, the value of $\tilde{k}_r$ also affects the values of $\tilde{\gamma}_1$ and $\tilde{\gamma}_2$. Indeed, according to Fig. 3, reducing $\tilde{k}_r$ leads to a thinner dimensionless gap $\tilde{z}_0$, which, in turn, significantly increases the elongation of the bristle in the radial direction (notably, for $\tilde{z}_0 \to 0$, both the friction force and the radial elastic reaction force act in the x,y plane). Under these conditions, according to Eq. (7), a long-lasting " sticky" phase occurs between the bristle and the slab (i.e., $V_R \approx 0$ for a relatively long time interval), thus leading to " static-like" conditions, with

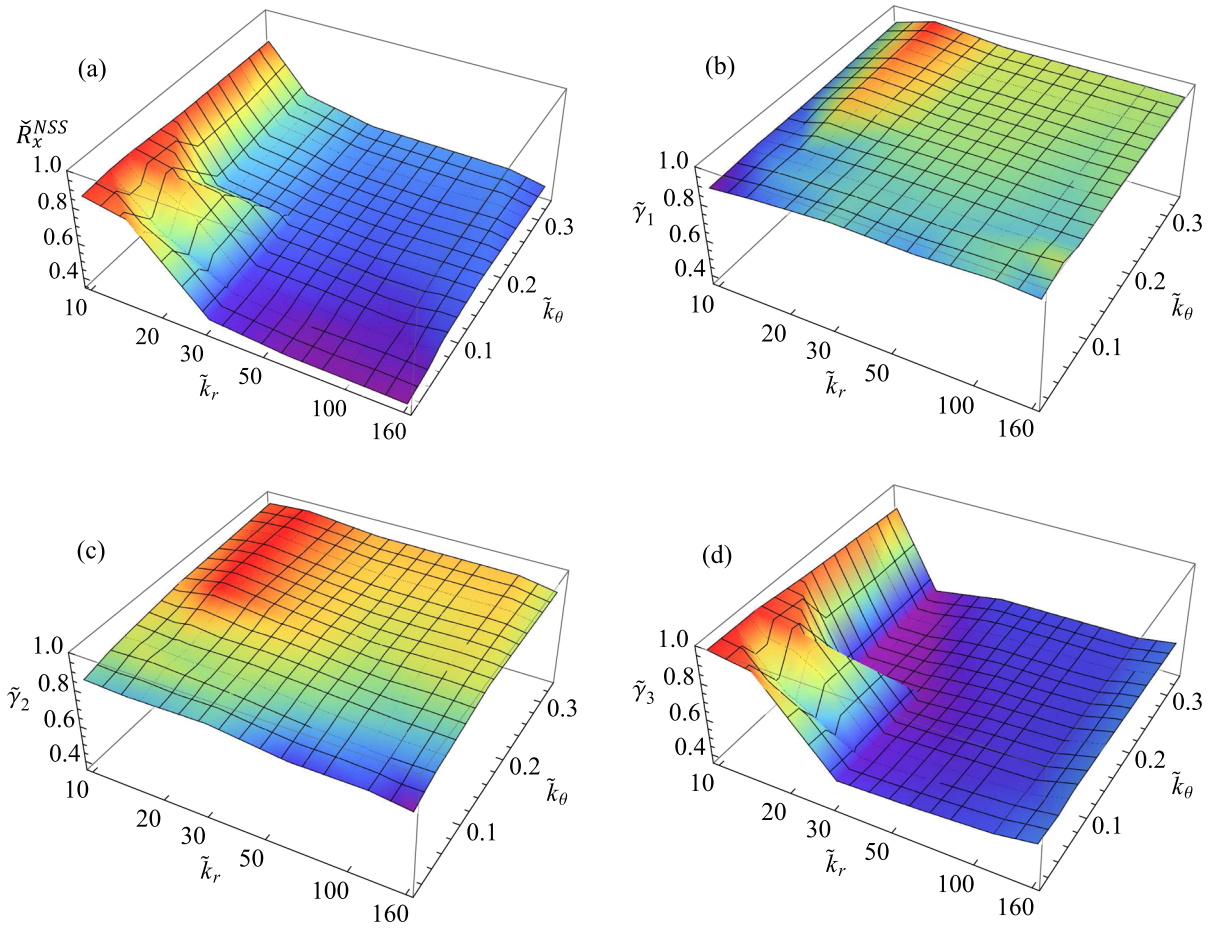

Fig. 4 The frictional response of the bristles array with *NSS* friction model. A 3D representation of the normalized friction force component in the *x-direction* $\check{R}_x^{\mathrm{NSS}}$ (**a**), and the dimensionless parameters $\tilde{\gamma}_1$ (**b**), $\tilde{\gamma}_2$ (**c**), $\tilde{\gamma}_3$ (**d**), as functions of the radial $\tilde{k}_r$ and torsional $\tilde{k}_\theta$ bristles stiffnesses. Results are for $\tilde{k}_\varphi = 1.9$ and $\tilde{R}_n/N_{c,0} = 2$

low friction force and $\tilde{\gamma}_1$ values. It is worth to note that a similar mechanism of friction reduction has been numerically predicted in Ref. [26], and experimentally observed in Refs. [41,42] for interfaces with compliant polymeric nanofibers with high aspect-ratio. Moreover, increasing $\tilde{k}_r$ also leads to a reduction of the lever arm s of the friction force F_f acting on each bristle in the x,y plane (see Fig. 1c). Since the modal mass associated with the azimuthal degree of freedom θ can roughly be estimated as $m_\theta \approx ms^2$, increasing $\tilde{k}_r$ eventually leads to higher transverse vibration frequency (i.e., in the x,y plane), thus reducing both $\tilde{\gamma}_2$ and $\check{R}_x^{\mathrm{NSS}}$. In conclusion, the analysis of the friction reduction mechanisms described by $\tilde{\gamma}_1, \tilde{\gamma}_2, \tilde{\gamma}_3$ indicates that increasing $\tilde{k}_r$ leads to thick gaps (i.e., large value of $\tilde{z}_0$), which eventually entails lower friction opposing the slab motion.

The results presented in Fig. 4 suggest that the frictional behavior of the bristles array is less sensitive to the value of $\tilde{k}_\theta$. Indeed, $\tilde{k}_\theta$ mainly affects the friction reduction mechanism relying on transverse vibration superimposed on the macroscopic slab motion. Under a given friction force F_f acting on the bristle, reducing $\tilde{k}_\theta$ entails two competing effects on $\tilde{\gamma}_2$ and $\check{R}_x^{\mathrm{NSS}}$: on one hand, according to the previous discussion, a reduction of the transverse vibration frequency occurs, which may induce higher values of $\tilde{\gamma}_2$ and $\check{R}_x^{\mathrm{NSS}}$; on the other hand, it also entails wider amplitude of transverse oscillation, thus suggesting a possible reduction of $\tilde{\gamma}_2$ and $\check{R}_x^{\mathrm{NSS}}$. Figure 4c shows that reducing $\tilde{k}_\theta$ leads to an overall reduction of the normalized friction force component $\check{R}_x^{\mathrm{NSS}}$, thus indicating that the dominant mechanism is the latter one.

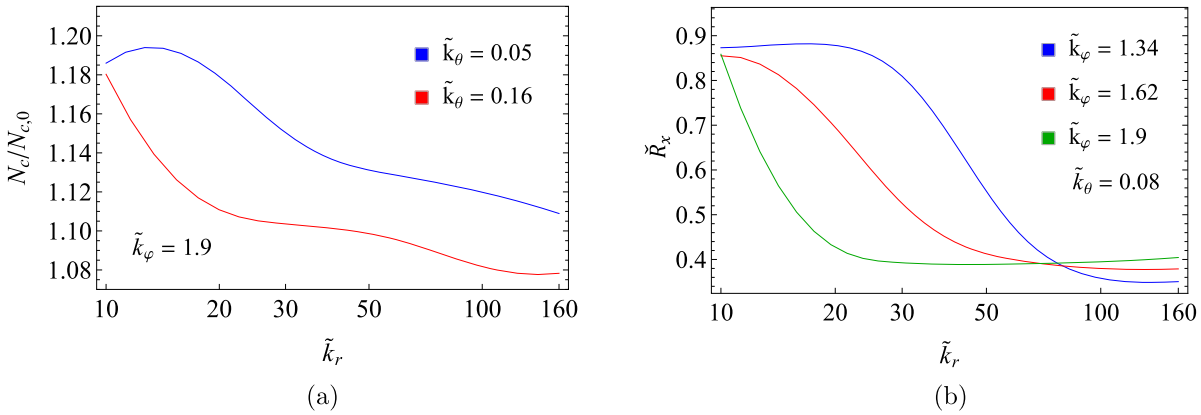

Fig. 5 The normalized number $N_c/N_{c,0}$ of contacting bristles (**a**), and the normalized friction force component $\check{R}_x^{\mathrm{NSS}}$ (**b**) as functions of the blisters radial stiffness $\tilde{k}_r$, for different values of the blister bending stiffness $\tilde{k}_\varphi$. Results refer to the *NSS* friction model, with $\tilde{R}_n/N_{c,0} = 2$

The effect of the bristle bending stiffness $\tilde{k}_\varphi$ on the normalized friction force component $\check{R}_x^{\mathrm{NSS}}$ is, instead, explored in Fig. 5b. We observe that, projecting Eq. (13) along $\hat{\mathbf{k}}$, the elastic reaction forces related to bristle axial compression (governed by $\tilde{k}_r$) and polar bending (governed by $\tilde{k}_\varphi$) synergically contribute to balance the normal force $\tilde{F}_n \approx \tilde{R}_n/N_{c,0}$ acting on each bristle. Therefore, under a given normal force, in order to keep constant the dimensionless gap $\tilde{z}_0$, reducing $\tilde{k}_\varphi$ requires increasing $\tilde{k}_r$. Now, recalling that $\check{R}_x^{\mathrm{NSS}}$ monotonically decreases with $\tilde{z}_0$ increasing (see previous discussion about $\tilde{\gamma}_3$ behavior), the results shown in Fig. 5b qualitatively indicate that reducing $\tilde{k}_\varphi$ shifts the same frictional response of the interface toward higher values of $\tilde{k}_r$.

3.2 *Amontons-Coulomb* model

In this section, we investigate the interface behavior assuming local *Amontons-Coulomb* friction, i.e., Equation (8), with $\mu_c = 1$. Also, a detailed analysis of the results sensitivity to the value of μ_c is provided in what follows. Notably, in this case the local friction force does not depend on the actual contact area between the bristles tips and the slab; therefore, only two of the three previously defined friction reduction mechanisms are effective: the velocity-dependent modulation of the friction force F_f; and the misalignment between the friction force and slab velocity directions, due to bristle *in-plane* transverse vibration. Respectively, these are quantified by the dimensionless parameters $\tilde{\gamma}_1$ and $\tilde{\gamma}_2$ defined through Eqs. (24, 25).

The array behavior is shown in Fig. 6 in terms of normalized friction force component $\check{R}_x^C$ and dimensionless parameters $\tilde{\gamma}_1$ and $\tilde{\gamma}_2$ as functions of both the dimensionless radial and azimuthal stiffness $\tilde{k}_r$ and $\tilde{k}_\theta$. As expected, the trends in Fig. 6 are qualitatively similar to those reported in Fig. 4a–c for interface with local *NSS* friction. Indeed, the effects of $\tilde{k}_r$ and $\tilde{k}_\theta$ on $\tilde{\gamma}_1$ and $\tilde{\gamma}_2$, as qualitatively discussed in the previous section, do not strictly depend on the specific local friction mechanics. Nonetheless, since friction control mechanism related to the local contact area is here missing, we observe that the friction mitigation reported in Fig. 6a with $\tilde{k}_r$ increasing presents a smoother trend, compared to the case of *NSS* local friction model.

This result is even more clearly shown in Fig. 7 where, varying $\tilde{k}_r$, we compare the interface responses related to *NSS* and *Amontons-Coulomb* local friction models. In Fig. 7a, the comparison shows a steep reduction of $\check{R}_x$ in the case of *NSS* friction; whereas, in the case of *Amontons-Coulomb* friction, the reduction of $\check{R}_x$ occurs over a broader range of $\tilde{k}_r$. Figure 7b confirms that $\tilde{z}_0$ plays a key role in determining the interface frictional behavior, with larger values of $\tilde{z}_0$ entailing lower values of $\check{R}_x$, regardless of the specific friction model. These latter results prove that the mechanism of friction control highlighted in the present study are poorly affected by the local friction model. Since the latter is usually scale dependent (i.e., *NSS* is best suited for soft micro-scale interfaces, and *Amontons-Coulomb* for hard macro-ones), our qualitative conclusion can reasonably be extended to bristle-like structured inter-

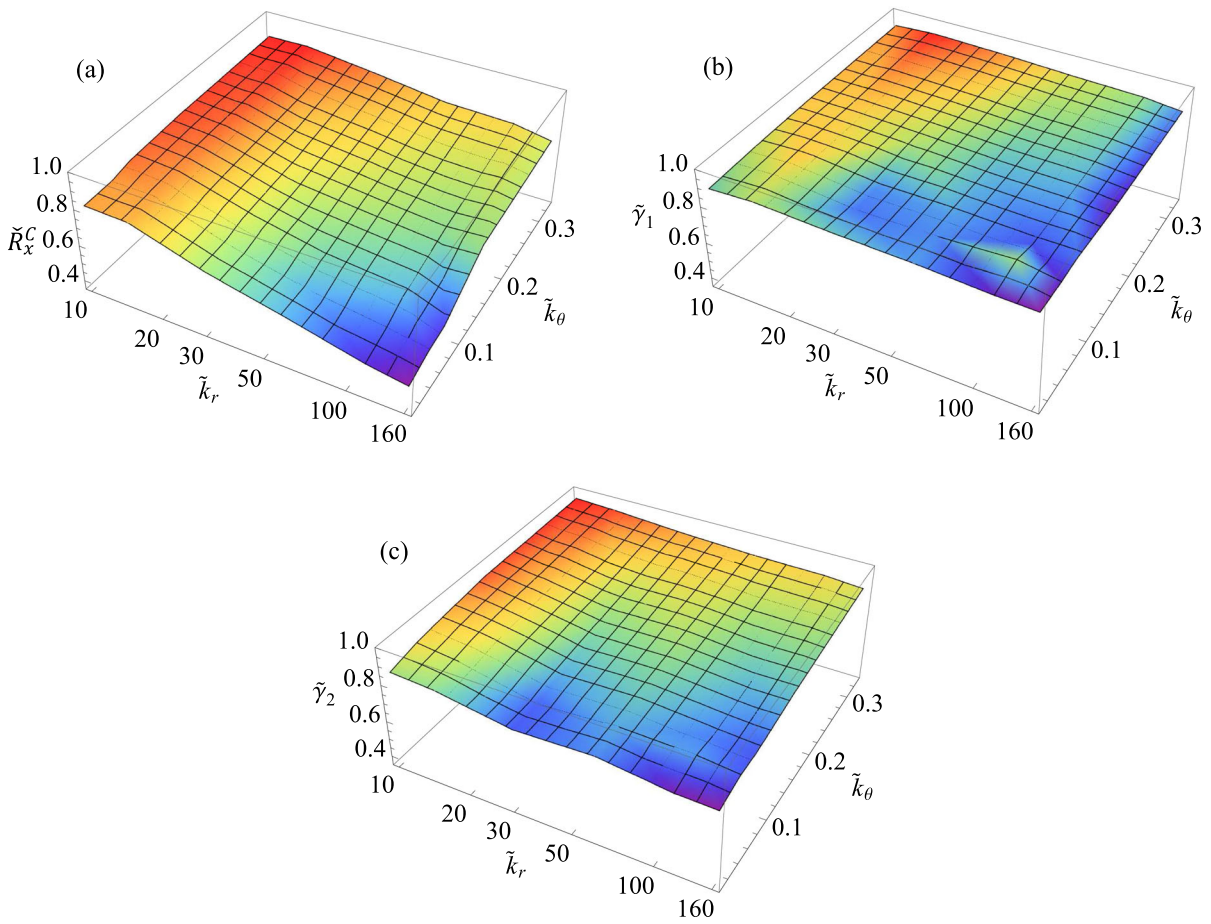

Fig. 6 The frictional response of the bristles interface with local *Amontons-Coulomb* friction model. A 3D representation of the normalized friction force component in the *x-direction* $\check{R}_x^C$ (**a**), and the dimensionless parameters $\tilde{\gamma}_1$ (**b**), $\tilde{\gamma}_2$ (**c**), as functions of the radial $\tilde{k}_r$ and torsional $\tilde{k}_\theta$ bristles stiffnesses. Results are for $\tilde{k}_\varphi = 1.9$ and $\tilde{R}_n / N_{c,0} = 2$

face ranging over a broad scales spectrum, such as soft polymeric micro-fibers [41,42] and metallic brushes [28]. Of course, at the nano-scale, frictional interactions may become discrete (i.e., atomistic friction), thus entailing different friction mechanisms [43,44] (e.g., adsorption, inter-locking, etc.) which could eventually alter the results.

The effect of the local friction coefficient μ_c on the overall interface frictional response is investigated in Fig. 8, for two different values of $\tilde{k}_r$. According to the results shown in Fig. 6a, we confirm that, at low values of $\tilde{k}_r$, the structured interface generates a slightly lower normalized friction force component $\check{R}_x^C$ compared to the rigid case (see blue curve). Things change when considering interfaces of stiffer bristles, as the red curve in Fig. 8 shows that, in this case, increasing μ_c leads to a saturation of the friction force component R_x opposing to a slab motion, which keeps a constant value even for further increase of μ_c. Interestingly, these results seem to indicate that the maximum friction force opposing the slab motion is an intrinsic property of the interface, which depends on the geometry and elasticity of the interfacial features (i.e., on the dimensionless elastic bristle parameters), rather than on the local friction behavior and intensity. Such a result could be of key importance in several engineering applications involving sliding contacts with interfacial structures (e.g., brush seals, bio-inspired soft interfacial features): in these cases, indeed, the interface elastic parameters might be tuned in order to limit the

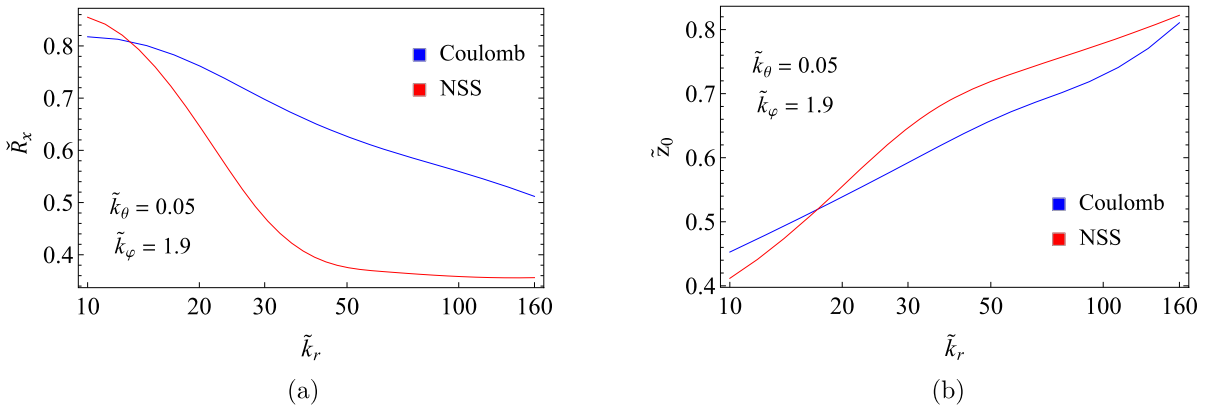

Fig. 7 The comparison between the bristles array behaviors associated to Coulomb and NSS friction models, referring to the normalized friction force component $\check{R}_x$ (**a**), and the dimensionless slab sliding height $\tilde{z}_0$ (**b**) as functions of the blisters radial stiffness $\tilde{k}_r$. Results are for $\tilde{R}_n/N_{c,0} = 2$

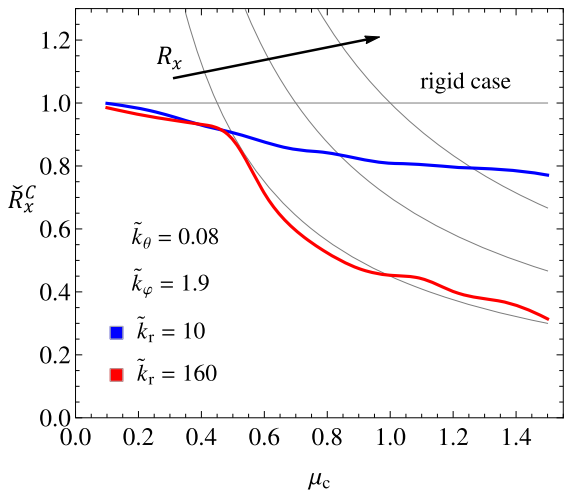

Fig. 8 The component in the *x-direction* $\check{R}_x^C$ of the normalized friction force opposing the slab sliding as a function of the local Coulomb friction coefficient μ_c at the bristles-slab interface. In the same figure, gray lines represent the $\check{R}_x^C$ trends related to the limiting rigid case and constant friction force R_x opposing the slab motion. Results refer to $\tilde{R}_n/N_{c,0} = 2$

maximum friction force, regardless of the specific local frictional behavior.

4 Conclusions

In this work, we focus on a structured interface with a lattice of bristle-like elastic features attached to a rigid still foundation in steady sliding contact with a sliding slab. Due to the time-varying normal and friction forces, complex bristle dynamics occurs during the contact, which may eventually alter the overall interface frictional behavior, i.e., macroscopic friction opposing the moving slab. We assumed two different local friction models at the interface between bristles tips and the moving slab: the well-known *Amontons-Coulomb* friction model, commonly adopted for stiff materials; and the *Nominal Shear Stress* model, usually applied to soft polymers. Notably, the latter model predicts the friction force as a nonlinear function of the local normal force.

Results show that both the friction models share two physical mechanisms of possible reduction of the overall interface friction, which arises due to local effects in the bristles dynamics: the local friction force modulation as a function of the relative velocity between the bristles tips and the moving slab; and the misalignment between the local friction force direction and the slab sliding direction. Moreover, due to the nonlinear effect of the local normal force acting on each bristle on the local friction force, the *NSS* friction model also offers an additional mechanism of possible friction reduction.

We report that increasing the axial (elongation) and polar (bending) stiffness of the blister leads to a significant reduction of the friction force opposing the slab motion. Similarly, also reducing the azimuthal (i.e., *in-plane* bending) stiffness of the bristles reduces the overall interfacial friction due to the emergence of self-excited *in-plane* transverse vibrations. Interestingly, since most of the physics behind the reported fric-

tion reduction is common across the two local friction models, these results appear qualitatively independent on the specific frictional interactions occurring between the surfaces. This makes the results peculiarly robust and independent of the problem scale, thus allowing for a generalization of the mechanisms of friction control in structured interfaces to several engineering application (e.g., brush seals in electric motors, and bio-inspired micro-fibers coatings).

Acknowledgements The authors acknowledge support from the Italian Ministry of Education, University and Research (MIUR) under the program "Departments of Excellence" (L.232/2016).

Author contributions All authors have contributed equally to this work.

Funding Open access funding provided by Politecnico di Bari within the CRUI-CARE Agreement. This project has received funding from the European Union's Horizon 2020 research and innovation programme under the Marie Skłodowska- Curie Grant Agreement No. 845756 (N.M. Individual Fellowship). This work was partly supported by the Italian Ministry of Education, University and Research under the Programme " Progetti di Rilevante Interesse Nazionale (PRIN)," Grant Protocol 2017948, Title: Foam Airless Spoked Tire – FASTire (G.C.).

Data availability Data sharing not applicable to this article as no datasets were generated or analyzed during the current study.

Declarations

Conflict of interest The authors have no relevant financial or non-financial interests to disclose.

Appendix A: Forces acting on the rigid slab

In this section, we define a procedure to calculate the reaction force $\mathbf{R}(t)$ acting on the slab to balance the time-varying actions produced by the time-varying set of bristles in contact with the slab, by summing up the specific normal $F_n(t)$ and friction $F_f(t)$ force resulting from each bristle. Notably, since all the bristles composing the array share the same elastic and frictional properties, and since the array is homogeneous with respect to the initial undeformed angles θ_0 and φ_0, in the limit of sufficiently large N_c, we expect the slab to experience a steady mean force $\bar{\mathbf{R}}$, after a quick transient phase.

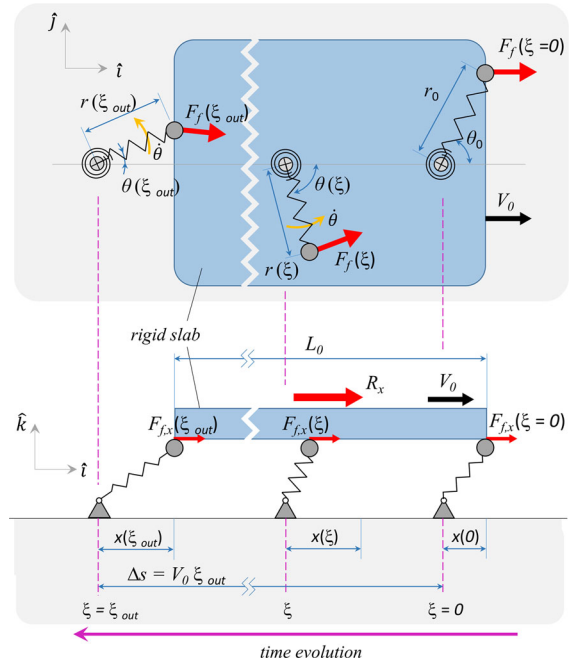

Fig. 9 A representation of the time evolution in the sliding process of a bristle against the rigid slab. Notably, $F_{f,x} = \mathbf{F}_f \cdot \hat{\imath}$

As shown in Fig. 9, due to the array spacing, successive rows of bristles come into contact with the rigid slab at different times. In this regard, we define two different time systems: (i) the global time system t, governing the slab sliding process (slab motion starts at $t = 0$); and (ii) the local bristle time system ξ_i associated with the generic ith bristle, which enters the contact with the slab leading edge at $\xi_i = 0$ and leaves the contact at the slab trailing edge at $\xi_i = \Delta\xi_i$. Therefore, referring to Fig. 9, we have

$$\xi_i = t - [h(i) - 1]\,\frac{\Delta}{V_0} \tag{A1}$$

where $h(i)$ is the bristle row containing the ith bristle, as shown in Fig. 1a. The dynamics of the generic ith bristle can be calculated by means of Eqs. (13, 17, 18),

whereas the contacting time $\Delta\xi_i$ can be calculated as

$$L_x = -\int_0^{\Delta\xi_i} d\xi \, (\mathbf{V}_R)_i \cdot \hat{\imath}. \tag{A2}$$

Moreover, since for $\xi_i < 0$ and $\xi_i > \Delta\xi_i$ no interaction occurs between the generic ith bristle and the rigid slab (i.e., $(F_n)_i = \left(F_f\right)_i = 0$), the momentum equilibrium of the slab at a generic time t is given by

$$\mathbf{R}\,(t) = \sum_{i \in \Omega(t)} \left[\mathbf{F}_n\,(\xi) + \mathbf{F}_f\,(\xi)\right]_i \tag{A3}$$

where $\Omega\,(t)$ is the set of $N_c\,(t)$ bristles in contact with the slab at time t, and the time-transformation $\xi_i \rightarrow t$ is provided by Eq. (A1).

Finally, the mean reaction force acting on the slab can be calculated as

$$\bar{\mathbf{R}} = \frac{1}{t_2 - t_1} \int_{t_1}^{t_2} dt \mathbf{R}\,(t) \tag{A4}$$

where $t_1 \approx L_x / V_0$ is the time at which the transient effects can be neglected, and t_2 can be arbitrarily chosen provided that $t_2 \gg t_1$.

References

1. Campaná, C., Müser, M.H.: Practical Green's function approach to the simulation of elastic semi-infinite solids. Phys. Rev. B **74**(7), 075420 (2006)
2. Pastewka, L., Robbins, M.O.: Contact between rough surfaces and a criterion for macroscopic adhesion. Proc. Natl. Acad. Sci. **111**(9), 3298–3303 (2014)
3. Menga, N., Afferrante, L., Demelio, G.P., Carbone, G.: Rough contact of sliding viscoelastic layers: numerical calculations and theoretical predictions. Tribol. Int. **122**, 67–75 (2018)
4. Persson, B.N.J.: Theory of rubber friction and contact mechanics. J. Chem. Phys. **115**, 3840–3861 (2001)
5. Persson, B.N., Albohr, O., Tartaglino, U., Volokitin, A.I., Tosatti, E.: On the nature of surface roughness with application to contact mechanics, sealing, rubber friction and adhesion. J. Phys. Condens. Matter **17**(1), R1 (2004)
6. Menga, N., Putignano, C., Carbone, G., Demelio, G.P.: The sliding contact of a rigid wavy surface with a viscoelastic half-space. Proc. R. Soc. A **470**(2169), 20140392 (2014)
7. Menga, N., Bottiglione, F., Carbone, G.: The nonlinear dynamic behavior of a Rubber-Layer Roller Bearing (RLRB) for vibration isolation. J. Sound Vib. **463**, 114952 (2019)
8. Menga, N., Bottiglione, F., Carbone, G.: Nonlinear viscoelastic isolation for seismic vibration mitigation. Mech. Syst. Signal Process. **157**, 107626 (2021)
9. Menga, N.: Rough frictional contact of elastic thin layers: the effect of geometrical coupling. Int. J. Solids Struct. **164**, 212–220 (2019)
10. Menga, N., Carbone, G., Dini, D.: Exploring the effect of geometric coupling on friction and energy dissipation in rough contacts of elastic and viscoelastic coatings. J. Mech. Phys. Solids **148**, 104273 (2021)
11. Kumar, V.C., Hutchings, I.M.: Reduction of the sliding friction of metals by the application of longitudinal or transverse ultrasonic vibration. Tribol. Int. **37**(10), 833–840 (2004)
12. Tsai, C.C., Tseng, C.H.: The effect of friction reduction in the presence of in-plane vibrations. Arch. Appl. Mech. **75**(2), 164–176 (2006)
13. Wang, P., Ni, H., Wang, R., Li, Z., Wang, Y.: Experimental investigation of the effect of in-plane vibrations on friction for different materials. Tribol. Int. **99**, 237–247 (2016)
14. Persson, B.N.J.: Theory of friction: Stress domains, relaxation, and creep. Phys. Rev. B **51**(19), 13568 (1995)
15. Persson, B.N., Albohr, O., Mancosu, F., Peveri, V., Samoilov, V.N., Sivebæk, I.M.: On the nature of the static friction, kinetic friction and creep. Wear **254**(9), 835–851 (2003)
16. Dahl, P.R.: A solid friction model. Aerospace Corp El Segundo Ca (1968)
17. Piatkowski, T.: Dahl and LuGre dynamic friction models—the analysis of selected properties. Mech. Mach. Theory **73**, 91–100 (2014)
18. Jadav, P.U., Amali, R., Adetoro, O.B.: Analytical friction model for sliding bodies with coupled longitudinal and transverse vibration. Tribol. Int. **126**, 240–248 (2018)
19. Gutowski, P., Leus, M.: The effect of longitudinal tangential vibrations on friction and driving forces in sliding motion. Tribol. Int. **55**, 108–118 (2012)
20. Gutowski, P., Leus, M.: Computational model for friction force estimation in sliding motion at transverse tangential vibrations of elastic contact support. Tribol. Int. **90**, 455–462 (2015)
21. Al-Bender, F., Lampaert, V., Swevers, J.: Modeling of dry sliding friction dynamics: From heuristic models to physically motivated models and back. Chaos Interdiscip. J. Nonlinear Sci. **14**(2), 446–460 (2004)
22. Al-Bender, F., Lampaert, V., Swevers, J.: The generalized Maxwell-slip model: a novel model for friction simulation and compensation. IEEE Trans. Autom. Control **50**(11), 1883–1887 (2005)
23. Olami, Z., Feder, H.J.S., Christensen, K.: Self-organized criticality in a continuous, nonconservative cellular automaton modeling earthquakes. Phys. Rev. Lett. **68**(8), 1244 (1992)
24. Giacco, F., Ciamarra, M.P., Saggese, L., de Arcangelis, L., Lippiello, E.: Non-monotonic dependence of the friction coefficient on heterogeneous stiffness. Sci. Rep. **4**(1), 1–4 (2014)
25. Costagliola, G., Bosia, F., Pugno, N.M.: A 2-D model for friction of complex anisotropic surfaces. J. Mech. Phys. Solids **112**, 50–65 (2018)
26. Menga, N., Bottiglione, F., Carbone, G.: Dynamically induced friction reduction in micro-structured interfaces. Sci. Rep. **11**(1), 1–12 (2021)
27. Basu, P., Datta, A., Loewenthal, R., Short, J., Johnson, R.: Hysteresis and bristle stiffening effects in brush seals. J. Propul. Power **10**(4), 569–575 (1994)

28. Stango, R.J., Zhao, H., Shia, C.Y.: Analysis of contact mechanics for rotor-bristle interference of brush seal. J. Trib. **125**(2), 414–421 (2003)
29. Abdel-Aal, H.A.: Functional surfaces for tribological applications: inspiration and design. Surf. Topogr. Metrol. Prop. **4**(4), 043001 (2016)
30. Wang, M., Chen, W., Zhao, J., Yu, L., Yan, S.: Hairy-layer friction reduction mechanism in the honeybee abdomen. ACS Appl. Mater. Interfaces **13**(21), 24524–24531 (2021)
31. Vorvolakos, K., Chaudhury, M.K.: The effects of molecular weight and temperature on the kinetic friction of silicone rubbers. Langmuir **19**(17), 6778–6787 (2003)
32. Ouyang, W., Ramakrishna, S.N., Rossi, A., Urbakh, M., Spencer, N.D., Arcifa, A.: Load and velocity dependence of friction mediated by dynamics of interfacial contacts. Phys. Rev. Lett. **123**(11), 116102 (2019)
33. Braun, O.M., Peyrard, M.: Dependence of kinetic friction on velocity: master equation approach. Phys. Rev. E **83**(4), 046129 (2011)
34. Kikuuwe, R., Takesue, N., Sano, A., Mochiyama, H., Fujimoto, H.: Fixed-step friction simulation: from classical Coulomb model to modern continuous models. In: 2005 IEEE/RSJ International Conference on Intelligent Robots and Systems, pp. 1009–1016. IEEE (2005)
35. Wang, D.: Study of Stick-Slip Friction between Steering Intermediate Shafts Using ADAMS-Simulink Co-Simulation (No. 2008-01-0496). SAE Technical Paper (2008)
36. Pennestrì, E., Rossi, V., Salvini, P., Valentini, P.P.: Review and comparison of dry friction force models. Nonlinear Dyn. **83**(4), 1785–1801 (2016)
37. Aita, Y., Asanuma, N., Takahashi, A., Mayama, H., Nonomura, Y.: Nonlinear friction dynamics on polymer surface under accelerated movement. AIP Adv. **7**(4), 045005 (2017)
38. Sivebæk, I.M., Samoilov, V.N., Persson, B.N.: Frictional properties of confined polymers. Eur. Phys. J. E **27**(1), 37–46 (2008)
39. Bowden, F.P., Tabor, D.: The Friction and Lubrication of Solids, vol. 1. Oxford University Press, Oxford (2001)
40. Brooks, L.E.E., Purdy, D.J., Edmonds, S.: Theoretical and experimental investigation into the interaction between a snowboard or ski and an artificial snow surface. Proc. Inst. Mech. Eng. C J. Mech. Eng. Sci. **225**(7), 1565–1578 (2011)
41. Lee, D.H., Kim, Y., Fearing, R.S., Maboudian, R.: Effect of fiber geometry on macroscale friction of ordered low-density polyethylene nanofiber arrays. Langmuir **27**(17), 11008–11016 (2011)
42. Kim, Y., Claus, R.K., Limanto, F., Fearing, R.S., Maboudian, R.: Friction characteristics of polymeric nanofiber arrays against substrates with tailored geometry. Langmuir **29**(26), 8395–8401 (2013)
43. He, G., Muser, M.H., Robbins, M.O.: Adsorbed layers and the origin of static friction. Science **284**(5420), 1650–1652 (1999)
44. Klemenz, A., Pastewka, L., Balakrishna, S.G., Caron, A., Bennewitz, R., Moseler, M.: Atomic scale mechanisms of friction reduction and wear protection by graphene. Nano Lett. **14**(12), 7145–7152 (2014)